Materials Science & Engineering A 645 (2015) 65–71

Contents lists available at ScienceDirect

Materials Science & Engineering A

journal homepage: www.elsevier.com/locate/msea

Fine-scale precipitation in the high-entropy alloy $Al_{0.5}CrFeCoNiCu$

E.J. Pickering*, H.J. Stone, N.G. Jones

Department of Materials Science and Metallurgy, University of Cambridge, 27 Charles Babbage Road, Cambridge CB3 0FS, UK

ARTICLE INFO

Article history:
Received 27 April 2015
Received in revised form
24 July 2015
Accepted 2 August 2015
Available online 4 August 2015

Keywords:
High-entropy alloys
Precipitation
Kinetics
Phase transformations
Electron microscopy

ABSTRACT

The high-entropy alloy $Al_{0.5}CrFeCoNiCu$ has been shown to consist of two stable, face-centred cubic solid solutions at temperatures approaching its solidus: one rich in Cr, Fe, Co & Ni (dendritic) and the other rich in Cu (interdendritic). While some studies have suggested that the high-temperature microstructure may be metastably retained to room temperature through rapid cooling, evidence of phase decomposition has also been reported. In this study, fine-scale precipitation has been observed in samples of $Al_{0.5}CrFeCoNiCu$ that have been rapidly cooled after casting, and water quenched following ageing for 1000 h at 1000 °C. Contrary to previous reports, in the as-cast state, the two face-centred cubic phases, as well as an $L1_2$ phase, were found in *both* dendritic and interdendritic areas, with the dendritic areas having undergone a spinodal decomposition. After ageing and quenching, $L1_2$ precipitates were found in both dendritic and interdendritic areas, and precipitates of the Cr-, Fe-, Co- and Ni-enriched face-centred cubic phase were found in the Cu-rich interdendritic regions. Given the nature of the heat treatments applied, the results suggest that precipitation in the alloy is rapid and cannot be avoided, even when the material is cooled quickly to room temperature.

1. Introduction

High-entropy alloys (HEAs) are commonly defined as materials that contain five or more elements in near-equiatomic ratios [1]. Such alloys have been referred to as 'high-entropy' because, in contrast to conventional alloys, their multi-principal component compositions theoretically deliver significantly higher entropies of mixing. It was initially proposed that this high mixing entropy may be sufficient to stabilise solid solutions in preference to intermetallic compounds, which might otherwise be expected to form [1]. However, a recent study has suggested that the likelihood of formation of strongly bonded intermetallic compounds increases with the number of alloying elements [2]. Judicious alloying is therefore required if intermetallic phase formation is to be avoided.

Importantly, it has been suggested that HEAs comprising compositionally complex solid solutions may possess superior mechanical properties and enhanced phase stability, compared to their conventional counterparts. This has been attributed to the local distortions of the crystal caused by the presence of elements with different atomic radii. These distortions have been hypothesised to impede dislocation motion and atomic diffusion [1,3,4]. In addition, it has also been suggested that the variation in bonding potential energy experienced by an atom in moving from site to site results in reduced rates of substitutional diffusion [4].

The phase equilibria and properties of the $Al_xCrFeCoNiCu$ system have been widely investigated [1,5–11], with $Al_{0.5}CrFeCoNiCu$ receiving particular attention [12–18]. The original investigation of $Al_{0.5}CrFeCoNiCu$ reported the presence of two face-centred cubic (*fcc*, A1 in Strukturbericht notation) phases below the solidus temperature in the as-cast condition: one constituting the dendritic material and the other the interdendritic material. At lower temperatures, the dendritic *fcc* phase was reported to order fully to an $L1_2$ structure [12]. The majority of subsequent studies have confirmed the presence of a miscibility gap in the *fcc* solid solution below the solidus temperature [13–15], but the nature of the $L1_2$ formation is disputed. Some studies have suggested that no *fcc* ordering is involved and that the $L1_2$ phase forms directly below the solidus at the same time as the two *fcc* phases [14]. In contrast, other studies have demonstrated that the $L1_2$ phase only precipitates in the dendritic *fcc* phase after cooling to lower temperatures, i.e., that the *fcc* ordering is partial [15,16]. One of the most recent $Al_{0.5}CrFeCoNiCu$ studies identified only one *fcc* phase alongside an $L1_2$ phase in melt-spun material [18], in agreement with the full *fcc* → $L1_2$ ordering proposed originally. Reports have also identified a Ni–Al-based B2 phase and a Cr–Co-Fe-based σ phase in the alloy, following prolonged exposures at temperatures in the range 700–1000 °C [14,16].

Studies of $Al_xCrFeCoNiCu$ alloys with higher aluminium contents ($x \geq 1$) have identified the occurrence of spinodal decomposition and ordering of the dendritic constituent to form a coherent mixture of A2 and B2 phases, accompanied by precipitation

* Corresponding author. Fax: +44 1223 334567.
E-mail address: ejp57@cam.ac.uk (E.J. Pickering).

http://dx.doi.org/10.1016/j.msea.2015.08.010

of Cu-rich particles [12,8,11]. In this study, high-resolution electron microscopy has been used to show, for the first time, that a spinodal decomposition also occurs in the dendritic constituent of $Al_{0.5}CrFeCoNiCu$, leading to the formation of two *fcc* phases, following rapid cooling from the molten state. In addition, nano-scale *fcc* precipitates were observed in the interdendritic regions in the as-cast state, as well as after ageing and quenching. $L1_2$ precipitates were also observed, consistent with previous reports [15,16]. Notably, the $L1_2$ precipitates were not uniquely confined to either the dendritic or interdendritic areas, but were identified in both regions in both the as-cast state and after ageing and quenching.

2. Experimental

An ingot of $Al_{0.5}CrFeCoNiCu$ weighing 40 g was prepared via arc melting in an inert atmosphere from elemental metals with 99.95% purity. To increase compositional homogeneity, the ingot was inverted and remelted five times. A short section, approximately 10 mm long, was cut from the as-cast ingot, encapsulated in an evacuated argon-backfilled quartz ampoule, and heat treated at 1000 °C for 1000 h, before quenching in water [15]. Specimens for transmission-electron microscopy (TEM) were prepared from both as-cast and heat-treated material by mechanically thinning slices to below 100 μm, spark eroding 3 mm discs, and ion-milling. The interdendritic constituent ion milled more readily than the dendritic material, and many interfaces between the two constituents were located in electron-transparent regions. Bright- and dark-field TEM images were taken using an FEI Tecnai Osiris microscope, using an accelerating voltage of 200 kV. The same microscope was also used for scanning-TEM (STEM) imaging, using a high-angle annular dark-field (HAADF) detector, as well as energy-dispersive X-ray mapping in STEM mode (STEM-EDX). X-ray diffraction (XRD) was carried out on a Bruker D8 ADVANCE instrument in Bragg–Brentano geometry using Cu K_α radiation. Data was collected between angles of 20 and 120° 2θ using a step size of 0.03° and a counting time of 3 s per step. Analyses of the resulting spectra were carried out in Wavemetrics Igor Pro and the peaks fitted with Gaussian functions that accounted for both $K_{\alpha1}$ and $K_{\alpha2}$ radiation.

3. Results

3.1. As-cast material

A region containing an interface between dendritic and interdendritic materials is shown in the bright-field image in Fig. 1a, in which the dendritic and interdendritic regions are labelled 1 and 2, respectively. The interdendritic material did not appear to be homogeneous and contained precipitates that had rectangular cross sections, which seemed to have similar crystallographic orientations. These precipitates are indicated with arrows in Fig. 1a. Electron diffraction patterns from both the dendritic and interdendritic regions are shown in Fig. 1b and c, respectively. Both patterns contained superlattice reflections consistent with the presence of an $L1_2$ phase, and showed that the dendritic and interdendritic regions had the same crystallographic orientation. Dark-field imaging, using the reflection indicated in Fig. 1b and c, enabled the $L1_2$ phase present in both regions to be examined using the same objective aperture location. The resulting image is shown in Fig. 1d, and confirmed the existence of $L1_2$ precipitates and an *fcc* matrix in both the dendritic and interdendritic regions, with the $L1_2$ precipitates appearing larger in the dendritic material. In the interdendritic material the larger rectangular-cross-sectioned precipitates did not appear bright in dark-field images using the superlattice reflections.

The interface between the dendritic and the interdendritic region shown in Fig. 1a was studied using HAADF STEM imaging, with the material oriented along a ⟨100⟩ zone axis, Fig. 2a. The selected-area diffraction patterns (SADPs) from this orientation, Fig. 2b and c, showed that the intensities of the $L1_2$ reflections were lower in the interdendritic material. This difference was more pronounced than in the diffraction patterns taken from the ⟨114⟩ orientation, Fig. 1b and c. STEM-EDX mapping was carried out on the area marked with a box in Fig. 2d, with the resulting elemental maps shown at the bottom of Fig. 2.

The STEM-EDX mapping revealed a nano-scale spinodal microstructure in the dendritic material, which is shown at higher magnification in Fig. 3. The EDX data indicated that the two components of the spinodal were rich in Cr, Co, Fe & Ni, and rich in Cu & Al, respectively. Cuboidal particles were also observed in the Cu-rich component, which were consistent in scale and morphology with the $L1_2$ precipitates seen in Fig. 1d. These particles were enriched in Ni & Al in comparison to the matrix and exhibited some solubility for Cu.

The precipitates present in the interdendritic material with rectangular cross-sections are located at the bottom of the EDX maps in Fig. 2. They were found to be rich in Cr, Co, Fe & Ni. This evidence, and their absence in superlattice dark-field imaging, suggested that they possessed an *fcc* crystal structure similar to that of the matrix. Also observed were the fine $L1_2$ precipitates identified in the dark-field image in Fig. 1d. These precipitates were enriched in Ni & Al, and showed some solubility for Cu, Co & Fe, but did not exhibit any enrichment in Cr.

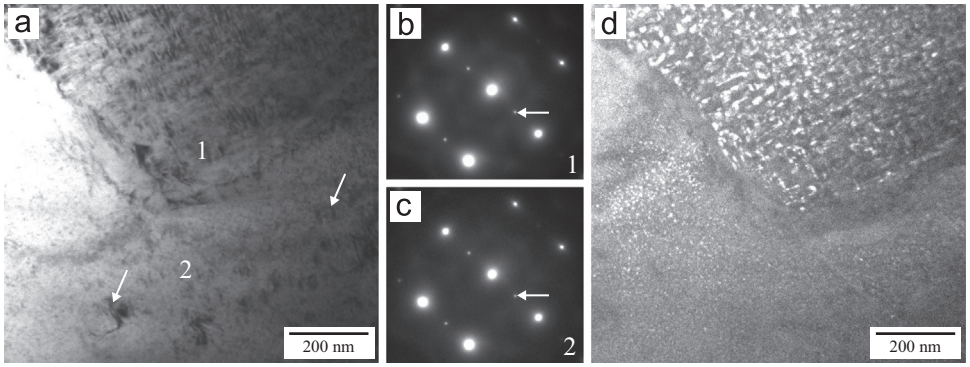

Fig. 1. TEM images and electron diffraction patterns from the as-cast material. (a) Bright-field image showing dendritic material (top, labelled 1) and interdendritic material (bottom, labelled 2). Precipitates with rectangular cross-sections are arrowed. (b) and (c) show ⟨114⟩ selected-area diffraction patterns (SADPs) from dendritic (1) and interdendritic (2) materials, respectively. (d) Dark-field image formed using the superlattice reflection indicated in the SADPs.

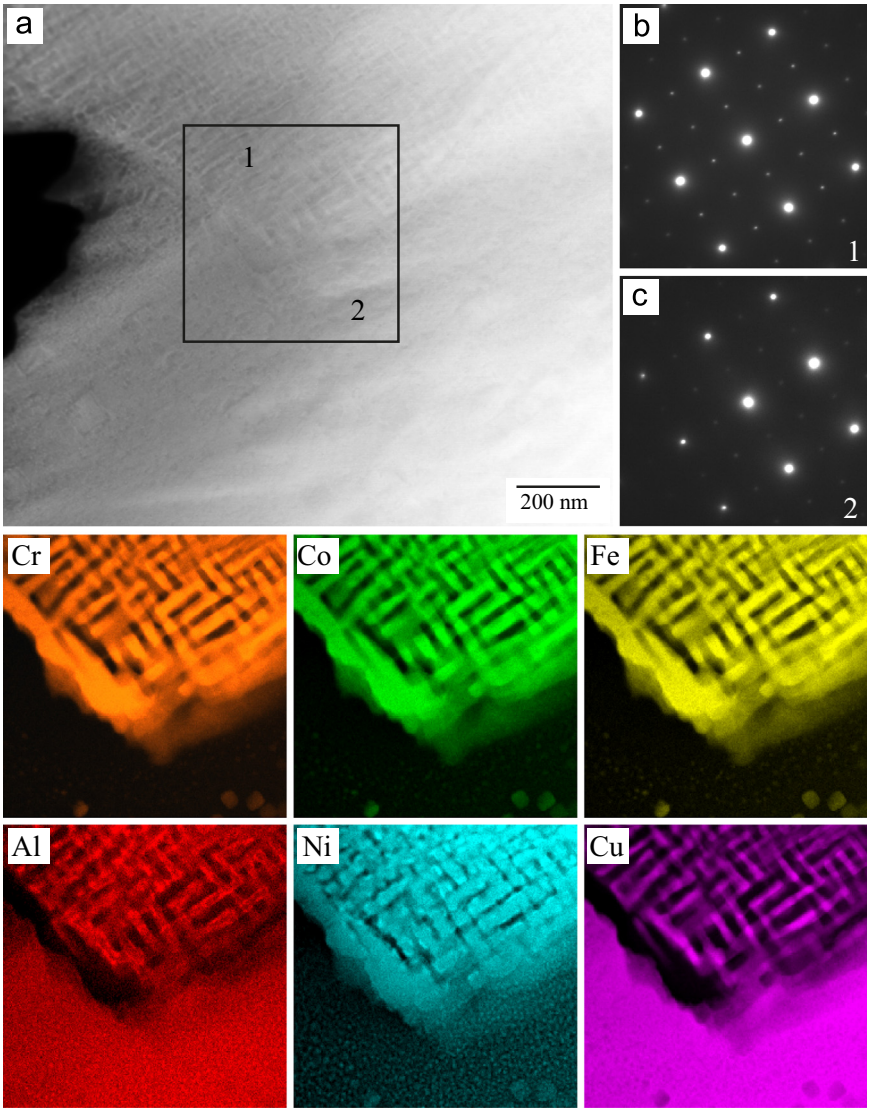

Fig. 2. The results of STEM imaging and STEM-EDX mapping of as-cast $Al_{0.5}CrFeCoNiCu$. (a) HAADF image of the region examined, with dendritic and interdendritic regions identified by 1 and 2, respectively. (b) and (c) ⟨100⟩ SADPs from dendritic (1) and interdendritic (2) materials, respectively. STEM-EDX maps for Cr, Co, Fe, Al, Ni & Cu, using the region indicated by the box in (a), are shown at the bottom of the figure.

3.2. 1000 °C 1000 h

A similar interface between dendritic and interdendritic regions was also analysed from material heat treated for 1000 h at 1000 °C. Fig. 4 shows the results of TEM, STEM-HAADF and STEM-EDX investigations, with the dendritic and interdendritic regions labelled 1 and 2, respectively. Bright-field TEM revealed relatively large precipitates in both the dendritic and the interdendritic material, labelled (i) and (ii) in Fig. 4a. The edges of the precipitates in the dendritic material appeared diffuse, while the precipitates present in the interdendritic material were more numerous and generally had a more defined shape. SADPs from both dendritic and interdendritic regions comprised predominantly *fcc* reflections, and demonstrated that both regions were very closely oriented, Fig. 4b and c. $L1_2$ superlattice reflections were again observed in the SADPs, and dark-field images were formed using the reflections marked by the arrows in Fig. 4b and c. The resulting dark-field image is shown in Fig. 4d and revealed extensive $L1_2$ precipitation in both dendritic and interdendritic areas, with the $L1_2$ precipitates in the interdendritic material appearing coarser. These coarse $L1_2$ precipitates were of a similar size to those observed in the Cu-rich spinodal material in the as-cast specimen. Interestingly, these precipitates were observed in the dendritic material in the as-cast state, not in the interdendritic material. It was noted that the intensity of the $L1_2$ reflections was diminished in the dendritic region (1), Fig. 4b. This may be indicative of a lower volume fraction of the $L1_2$ phase, but it could also have resulted from changes in the scattering contrast of the constituent elements, or have been a consequence of size-induced peak broadening. The large precipitates indicated in Fig. 4a appeared dark in dark-field imaging.

A STEM-HAADF image of the same interface is shown in Fig. 4e. EDX mapping was performed on the sub-region indicated by the box, and the elemental concentration maps obtained are presented at the end of Fig. 4. These revealed that the dendritic material was enriched in Cr, Co, Fe & Ni, and the interdendritic material was Cu-rich. Consistent with the results obtained from the as-cast material, the $L1_2$ precipitates in the dendritic material were enriched in Ni, Al & Cu relative to the matrix, while the $L1_2$ precipitates in the Cu-rich interdendritic material were enriched in Ni & Al. These interdendritic $L1_2$ precipitates showed some solubility for Co & Fe, but no detectable Cr. Another phase was also observed to be present in the interdendritic material, in the form of Cr-, Co- & Fe-rich precipitates that were smaller than the $L1_2$ particles. One

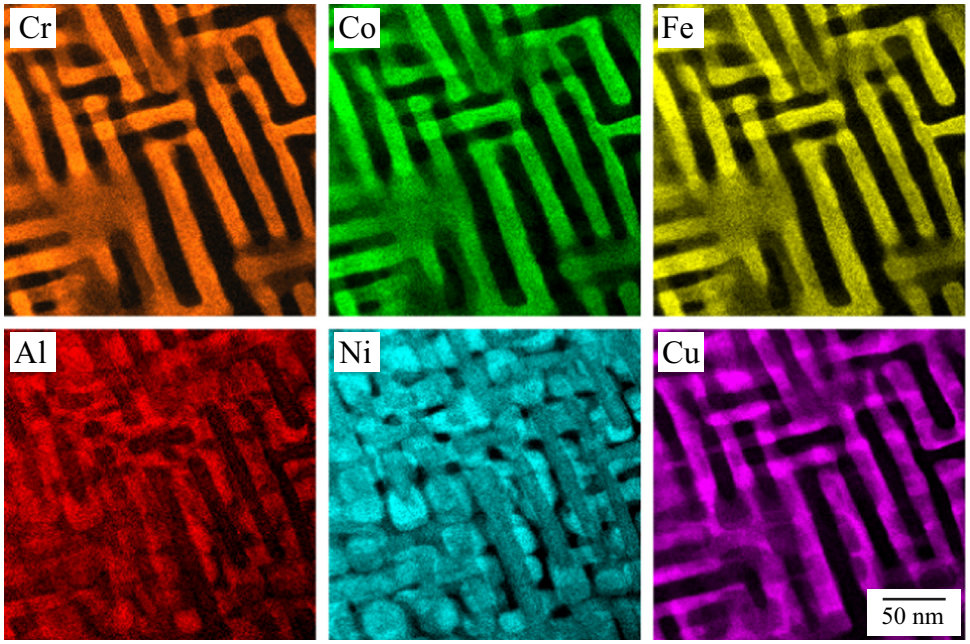

Fig. 3. STEM-EDX elemental composition maps of the dendritic material in the as-cast state, showing a spinodally decomposed structure, with $L1_2$ phase precipitation in the Cu-rich component.

of these precipitates is circled in the Cr, Co & Fe elemental maps. These small precipitates were not visible in bright-field imaging, and they did not appear bright in the dark-field images formed using the $L1_2$ superlattice reflections. These observations were consistent with the precipitates having an *fcc* structure.

STEM-EDX mapping revealed that the large precipitates observed in the bright-field images, labelled (i) and (ii) in Fig. 4a and e, were not the same in the dendritic and the interdendritic regions. The precipitates in the dendritic area, labelled (i), appeared to be Ni-rich, while the more well-defined precipitates in the interdendritic material, labelled (ii), were enriched in Cu. SADPs from regions containing these precipitates showed extra diffraction spots, indicating the presence of other phases besides the *fcc* and $L1_2$ phases described above. However, no information was gathered that could further elucidate their crystal structures.

4. Discussion

The results of this study confirm that two *fcc* phases are the predominant constituents in $Al_{0.5}$CrFeCoNiCu in both the as-cast state, and after ageing at 1000 °C for 1000 h followed by quenching. One is enriched in Cr, Co, Fe & Ni, which will subsequently be referred to as *fcc*1, while the other is enriched in Cu, with some solubility for Ni & Al, *fcc*2. Similar *fcc* phases have been identified in many of the previous $Al_{0.5}$CrFeCoNiCu studies [7,13–15] and the results obtained in this study are consistent with there being two stable *fcc* phases at temperatures immediately below the solidus, *fcc*1 and *fcc*2 [15,16]. On cooling from the solidus in the as-cast state, our findings suggest that *fcc*1, which is likely to have some solubility for Cu at high temperatures, spinodally decomposes into *fcc*1 and *fcc*2 at lower temperatures, relieving any Cu supersaturation. At lower temperatures still, the solubility of Ni & Al in *fcc*2 decreases and, as a result, a Ni- & Al-rich $L1_2$ phase precipitates. This occurs in the *fcc*2 present in both the spinodally decomposed dendritic material and in the interdendritic regions. The solubility of Cr, Co & Fe is also reduced in the interdendritic *fcc*2 at low temperatures, which leads to the precipitation of *fcc*1 as precipitates with rectangular cross-sections. This sequence is outlined in Fig. 5a. The size of the precipitates observed was consistent with the high cooling rate that would have been experienced by the as-cast material as a result of rapid cooling on a water-chilled copper hearth.

In the material aged at 1000 °C for 1000 h, experimental evidence suggests that the same two *fcc* phases are likely to have been stable at high temperature. However, the composition of both phases was altered subtly on ageing [12,13,15,16]. This appears to have eliminated the driving force for the spinodal decomposition of the dendritic material on cooling. However, this resulted in *fcc*1 retaining significant levels of Cu, Ni & Al, and these elements subsequently formed $L1_2$ precipitates at lower temperatures. In the interdendritic Cu-rich *fcc*2, a reduction in temperature again led to decreased solubility for the other alloying elements, resulting in the formation of $L1_2$ precipitates and *fcc*1. This sequence is shown in Fig. 5b. Importantly, the size of the precipitates was found to be consistent with the rapid cooling rates provided by water quenching.

The precipitation sequence for the aged material in Fig. 5 does not include the large Cu- and Ni-rich precipitates that were observed. These have been omitted as it is unclear at what point in the sequence they formed, and because their crystal structures have not been determined. Given their enrichment in *fcc*-forming elements, it is likely that the precipitates are also *fcc*, but this was not confirmed.

A previous study reported that the $L1_2$ precipitates found in aged $Al_{0.5}$CrFeCoNiCu were confined to the dendritic material [15]. Here, the use of high-resolution electron microscopy has demonstrated that the $L1_2$ precipitates are, in fact, formed in both dendritic and interdendritic materials, in the as-cast state as well as the aged condition. The same study also observed small deviations around 1000 °C in differential-scanning calorimetry thermograms for both as-cast and aged material, which could not be explained. In light of the results of this study, it is possible that these deviations were due to the dissolution of a second population of $L1_2$ precipitates in the interdendritic regions. An alternative possibility is that these deviations were caused by the dissolution of *fcc* precipitates that had formed in their counterpart *fcc* phase, for instance the circled precipitates in Fig. 4. A separate study of

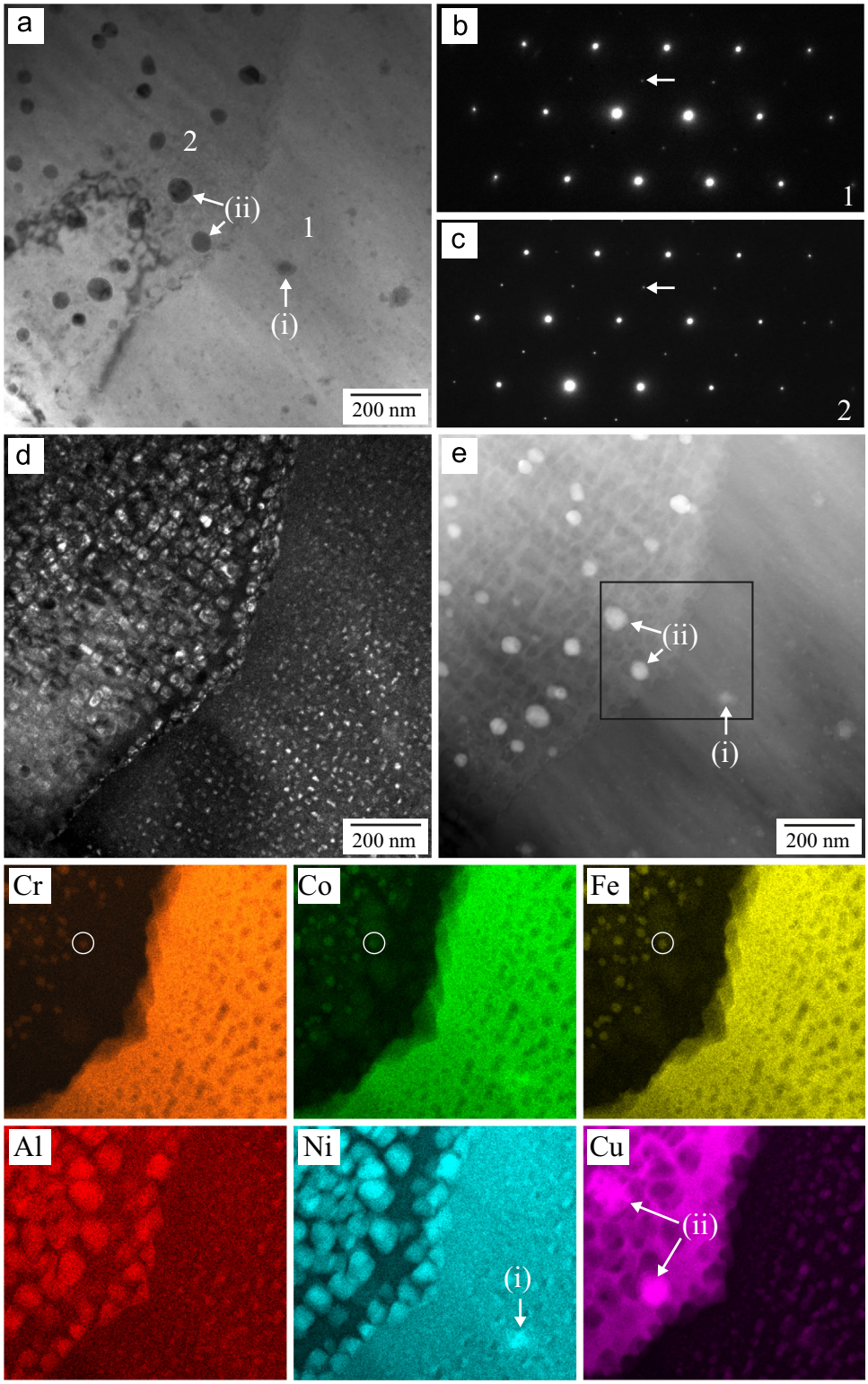

Fig. 4. (a) Bright-field TEM image of a region containing an interface between dendritic (1) and interdendritic (2) materials following exposure at 1000 °C for 1000 h and water quenching. The large precipitates in the dendritic and the interdendritic material are labelled (i) and (ii), respectively. (b) and (c) show ⟨110⟩ SADPs from dendritic (1) and interdendritic (2) areas, respectively. (d) Dark-field image of the area shown in (a) formed using the superlattice reflection arrowed in (b) and (c). (e) HAADF-STEM image of the area shown in (a). EDX maps, from the sub-region indicated by the box in (e), are shown at the bottom of the figure. The large precipitates labelled (i) and (ii) are indicated. An example of a small precipitate enriched in Cr, Co & Fe in the interdendritic area is circled.

$Al_{0.5}$CrFeCoNiCu has reported the presence of fine Cu-rich acicular precipitates in dendritic material following cooling from the liquid state at rates between 10 and 50 °C min^{-1} [17]. The results of the present study suggest that these precipitates were in fact part of the *fcc*1 → *fcc*1 + *fcc*2 spinodal decomposition, and that the scale of this spinodal decomposition increases with decreasing cooling rate.

Critically, the results of the present study are in contradiction with the findings of the original $Al_{0.5}$CrFeCoNiCu investigation [12], and also with one of the most recent studies of the alloy [18].

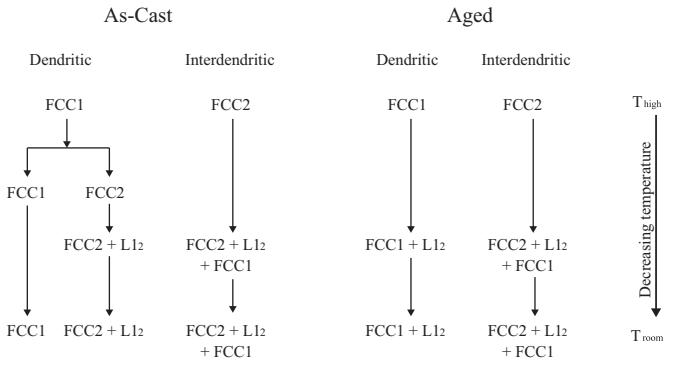

Fig. 5. A schematic representation of the precipitation sequence in $Al_{0.5}CrFeCoNiCu$ on cooling from casting, and during water quenching after exposure for 1000 h at 1000 °C.

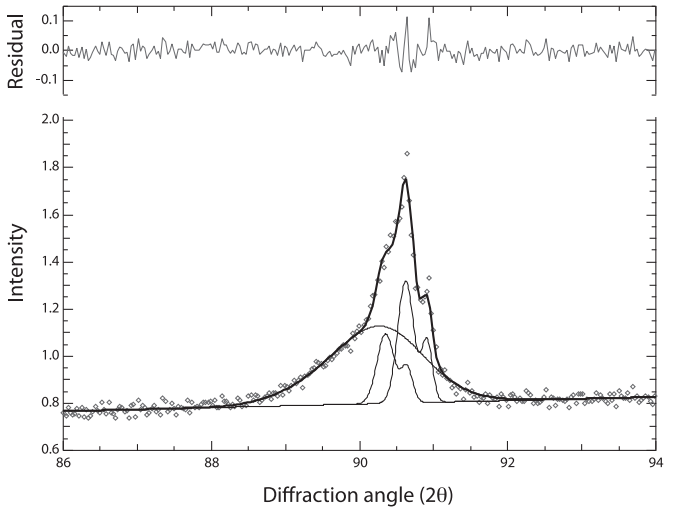

Fig. 6. XRD data showing the {311} reflection of $Al_{0.5}CrFeCoNiCu$ after heat treatment at 1000 °C for 1000 h and water quenching. The peak was fitted (bold line) using three Gaussian functions (thin lines below data) corresponding to the two *fcc* and the $L1_2$ phases. The $K_{\alpha1}$ and $K_{\alpha2}$ contributions were accounted for in all cases.

Both studies reported the existence of only one Cu-rich *fcc* phase, consistent with *fcc*2, and an $L1_2$ phase rich in Cr, Co, Fe & Ni in the material at low temperatures. These findings are surprising for two reasons. First, it is unusual to find an $L1_2$ phase rich in Cr, Co, Fe & Ni, as the elements are known to form stable *fcc* solid solutions in their respective ternary systems [19,20]. Second, the XRD patterns that are presented by the more recent study show pronounced asymmetry on a number of *fcc* peaks [18], which could be consistent with the presence of another *fcc* phase. XRD spectra from the two material conditions examined in the present manuscript were reported in a previous study, and showed evidence of at least two contributions to each *fcc* reflection [16]. Here, using a similar analysis approach with data obtained from a higher-resolution instrument, contributions from at least three phases were identified in the high-angle reflections, where peak separation is greatest. By way of example, the measured data and associated fit for the {311} reflections from a sample in the heat treated condition are shown in Fig. 6. The fit comprises three Gaussian functions, individually shown below the experimental data, which correspond to the two *fcc* phases and the $L1_2$ phases identified in Fig. 4. Unfortunately, the XRD patterns presented by the original study are not clear enough to discern whether asymmetry is present or not [12], but it is clear that in dark-field imaging the dendritic areas did not appear to comprise solely an $L1_2$ phase (Fig. 5 in [12]). Indeed, the dark features in the figure strongly resemble the results of spinodal decomposition seen in as-cast material here.

In explaining the results of $Al_{0.5}CrFeCoNiCu$ investigations, authors have often referred to the precipitation kinetics as being slow [12,14], following the belief that diffusion in HEAs is 'sluggish' [1,3,4]. However, the same studies present results that suggest quite the opposite; precipitation and spinodal structures are observed in as-cast $Al_xCrFeCoNiCu$ alloys, which are not consistent with slow kinetics [12,15,17,18]. The precipitation, and spinodal decomposition, observed in the alloy during rapid cooling in this study provides evidence that kinetics are not slow or 'sluggish'. Indeed, the $L1_2$ precipitates observed here are of the same scale that would be expected to form in Ni-based superalloys quenched from above their γ' solvus temperatures, suggesting that the precipitation characteristics are similar to existing alloys.

5. Summary and conclusions

The microstructure of $Al_{0.5}CrFeCoNiCu$ has been characterised using a combination of high-resolution electron microscopy techniques. Samples were studied in the as-cast state, and after ageing for 1000 h at 1000 °C followed by water quenching.

In the as-cast state, $Al_{0.5}CrFeCoNiCu$ was found to comprise two *fcc* phases and an $L1_2$ phase. One *fcc* phase was rich in Cr, Co, Fe & Ni, while the other was Cu rich. The $L1_2$ phase was rich in Ni & Al, with some solubility for Cu. The two *fcc* phases and the $L1_2$ phase were all present in both the dendritic and the interdendritic material. In the dendritic regions, the two *fcc* phases appeared to have formed through a spinodal decomposition.

After ageing for 1000 h at 1000 °C followed by water quenching, $L1_2$ precipitates were found in both the dendritic and interdendritic areas, with precipitates of the *fcc* phase rich in Cr, Co, Fe & Ni also appearing in the Cu-rich interdendritic material. Fine-scale precipitation was prevalent in both as-cast and aged material after rapid cooling, demonstrating that the precipitation kinetics were not slow, as is often claimed for HEAs.

Acknowledgements

The authors acknowledge funding from Rolls-Royce plc and the EPSRC under the Rolls-Royce/EPSRC Strategic Partnership (EP/M005607/1). Requests for access to the underlying research data should be directed to the corresponding author, and will be considered against commercial interests and data protection.

This paper can also be viewed at https://www.repository.cam.ac.uk/handle/1810/249206.

References

[1] J.-W. Yeh, S.-K. Chen, S.-J. Lin, J.-Y. Gan, T.-S. Chin, T.-T. Shun, C.-H. Tsau, S.-Y. Chang, Nanostructured high-entropy alloys with multiple principal elements: novel alloy design concepts and outcomes, Adv. Eng. Mater. 6 (2004) 299–303.

[2] O. Senkov, J. Miller, D. Miracle, C. Woodward, Accelerated exploration of multi-principal element alloys with solid solution phases, Nat. Commun. 6 (2015) (6529).

[3] J.-W. Yeh, Recent progress in high-entropy alloys, Ann. Chim.—Sci. Mater. 31 (2006) 633–648.

[4] M.-H. Tsai, J.-W. Yeh, High-entropy alloys: a critical review, Mater. Res. Lett. 2 (2014) 107–123.

[5] C.-J. Tong, M.-R. Chen, S.-K. Chen, J.-W. Yeh, T.-T. Shun, S.-J. Lin, S.-Y. Chang, Mechanical performance of the $Al_xCoCrCuFeNi$ high-entropy alloy system with multiprincipal elements, Metal. Mater. Trans. A 36A (2005) 1263–1271.

[6] M.-R. Chen, S.-J. Lin, J.-W. Yeh, S.-K. Chen, Y.-S. Huang, M.-H. Chuang, Effect of vanadium addition on the microstructure, hardness, and wear resistance of $Al_{0.5}CoCrCuFeNi$ high-entropy alloy, Metal. Mater. Trans. A 37A (2006)

1363–1369.
[7] J.-M. Wu, S.-J. Lin, J.-W. Yeh, S.-K. Chen, Y.-S. Huang, H.-C. Chen, Adhesive wear behavior of Al_xCoCrCuFeNi high-entropy alloys as a function of aluminum content, Wear 261 (2006) 513–519.
[8] C.-C. Tung, J.-W. Yeh, T.-T. Shun, S.-K. Chen, Y.-S. Huang, H.-C. Chen, On the elemental effect of AlCoCrCuFeNi high-entropy alloy system, Mater. Lett. 61 (2007) 1–5.
[9] W.-Y. Tang, J.-W. Yeh, Effect of aluminum content on plasma-nitrided Al_xCoCrCuFeNi high-entropy alloys, Metal. Mater. Trans. A 40A (2009) 1479–1486.
[10] R. Sriharitha, B. Murty, R. Kottada, Phase formation in mechanically alloyed Al_xCoCrCuFeNi (x 14 0.45, 1, 2.5, 5 mol) high entropy alloys, Intermetallics 32 (2013) 119–126.
[11] L. Santodonato, Y. Zhang, M. Feygenson, C. Parish, M. Gao, R. Weber, J. Neuefeind, Z. Tang, P. Liaw, Deviation from high-entropy configurations in the atomic distributions of a multi-principal-element alloy, Nat. Commun. 6 (2015) 5964.
[12] C.-J. Tong, Y.-L. Chen, S.-K. Chen, J.-W. Yeh, T.-T. Shun, C.-H. Tsau, S.-J. Lin, S.-Y. Chang, Microstructure characterization of Al_xCoCrCuFeNi high-entropy alloy system with multiprincipal elements, Metal. Mater. Trans. A 36A (2005) 881–893.
[13] C.-W. Tsai, Y.-L. Chen, M.-H. Tsai, J.-W. Yeh, T.-T. Shun, S.-K. Chen, Deformation and annealing behaviors of high-entropy alloy $Al_{0.5}$CoCrCuFeNi, J. Alloys Compds. 486 (2009) 427–435.
[14] C. Ng, S. Guo, J. Luan, S. Shi, C. Liu, Entropy-driven phase stability and slow diffusion kinetics in an $Al_{0.5}$CoCrCuFeNi high entropy alloy, Intermetallics 31 (2012) 165–172.
[15] N. Jones, J. Aveson, A. Bhowmik, B. Conduit, H. Stone, On the entropic stabilisation of an $Al_{0.5}$CrFeCoNiCu high entropy alloy, Intermetallics 54 (2014) 148–153.
[16] N. Jones, A. Frezza, H. Stone, Phase equilibria of an $Al_{0.5}$CrFeCoNiCu high entropy alloy, Mater. Sci. Eng. A 615 (2014) 214–221.
[17] N. Jones, K. Christofidou, H. Stone, Rapid precipitation in an $Al_{0.5}$CrFeCoNiCu high entropy alloy, Mater. Sci. Technol. 31 (2015) 1171–1177.
[18] X. Xu, P. Liu, S. Guo, A. Hirata, T. Fujita, T. Nieh, C. Liu, M. Chen, Nanoscale phase separation in a FCC-based CoCrCuFeNi$Al_{0.5}$ high-entropy alloy, Acta Mater. 84 (2015) 145–152.
[19] G. Raynor, V. Rivlin, Phase Equilibria in Iron Ternary Alloys, Institute of Metals, London, UK, 1988.
[20] K. Gupta, Phase Diagrams of Ternary Nickel Alloys, Indian Institute of Metals, Calcutta, India, 1990.